Available online at www.sciencedirect.com
ScienceDirect
Journal of Magnetic Resonance 184 (2007) 1–14
JMR Journal of Magnetic Resonance
www.elsevier.com/locate/jmr

HMQC and refocused-INEPT experiments involving half-integer quadrupolar nuclei in solids

J.P. Amoureux [a,*], J. Trebosc [a], J. Wiench [b], M. Pruski [b]

[a] UCCS, CNRS-8181, ENSCL-USTL, Fr-59652 Villeneuve d'Ascq, France
[b] Ames Laboratory, Iowa State University, Ames, IA 50011, USA

Received 17 July 2006; revised 14 September 2006
Available online 4 October 2006

Abstract

Hetero-nuclear coherence transfers in HMQC and refocused-INEPT experiments involving half-integer quadrupolar nuclei in solids are analyzed. 1D and 2D schemes are considered under MAS for the general case of multi-spin systems SI_n ($n \leqslant 4$), where S is an observed nucleus. These results are also discussed in the context of high-resolution schemes featuring MQMAS or STMAS. The theoretical predictions are verified experimentally in a series of 1D and 2D experiments performed at 9.4 and 18.8 T.

Keywords: Solid-state NMR; *J*-coupling; R-INEPT; HMQC; Quadrupolar nuclei; MAS; MQMAS; STMAS

1. Introduction

Scalar (J) couplings are due to interactions between nuclei that are indirectly transmitted through the electrons of the bonds. These interactions are undisturbed by molecular motions and thus, along with the chemical shifts, are commonly used in liquid state NMR for spectral assignments and for establishing through bond correlations between atoms [1]. In the solid state, J couplings are more difficult to observe directly, as they are obscured by the much stronger dipolar, chemical shift and quadrupolar contributions to the line-width. In relatively mobile solids, such as adamantane, the ^{13}C–^{1}H J multiplets were observed by combining magic angle spinning (MAS) with homo-nuclear ^{1}H–^{1}H radio frequency (RF) decoupling [2,3]. Direct detection of J multiplets was also reported in rigid systems with relatively large scalar couplings, provided that the other line broadening interactions could be sufficiently reduced [4–7]. The measurement and utilization of J couplings are nevertheless possible in cases where the splittings cannot be directly resolved in the spectra. For example, J coupling can be assessed from the time evolution of polarization build-up during INEPT experiments [6,8], by using the rotor-synchronized two-dimensional (2D) spin-echo method [9] and via REDOR-like approaches [10,11]. Other studies demonstrated the utility of hetero-nuclear J couplings for spectral editing in ordinary organic solids [12–15].

Further exploitation of scalar couplings in solids resulted in the development of 2D homo- and hetero-nuclear correlation J spectroscopy, which was for the most part inspired by the high-performance techniques known for solutions. The examples of homo-nuclear correlation included INADEQUATE [16–21], COSY [17,18,22] and TOBSY [23] experiments with ^{13}C, ^{15}N and ^{29}Si nuclei in a number of organic and inorganic materials. In hetero-nuclear correlation (HETCOR) NMR of solids, the coherence transfer is usually achieved through space via dipolar cross polarization (CP) [24–26] or TEDOR [27,28]. By using MAS in concert with various homo- and hetero-nuclear RF decoupling schemes, highly resolved through space correlation spectra can now be routinely obtained in chemical and bio-chemical compounds [26,29–31]. The first 2D J-resolved hetero-nuclear NMR experiments also used ^{1}H–^{13}C

* Corresponding author. Fax: +1 33 3 20 43 68 14.
E-mail address: jean-paul.amoureux@univ-lille1.fr (J.P. Amoureux).

1090-7807/$ - see front matter © 2006 Elsevier Inc. All rights reserved.
doi:10.1016/j.jmr.2006.09.009

CP coherence transfer [32] (or direct ^{13}C excitation [33]) and a combination of ^{1}H decoupling with rotor-synchronized refocusing at the ^{13}C frequency, to yield the ^{13}C multiplet structures. However, J couplings can be also used for hetero-nuclear mixing to generate 1D spectra or 2D maps of through-bond chemical shift correlations between spins, through various schemes that use direct (INEPT [12,13,34]) or indirect (HMQC [35]) detection.

Some of the most notable accomplishments of J spectroscopy in solids involve half-integer quadrupolar nuclei, in spite of the additional challenges posed by second-order quadrupolar broadening. J couplings were observed or measured in several molecular systems containing ^{23}Na, ^{27}Al, ^{31}P and ^{29}Si nuclei [6,7,36,37], and the MAS-based HETCOR spectra between ^{27}Al and ^{31}P in aluminophosphate $AlPO_4$-14 have been reported [34]. The HMQC HETCOR spectra were obtained between ^{31}P and ^{27}Al in aluminophosphates [36] and between ^{17}O and ^{27}Al in a glass [38]. More recently, a ^{27}Al–^{27}Al homo-nuclear correlation spectrum has been shown, obtained via J-mediated Al–O–P–O–Al transfer in $AlPO_4$-14 [39]. Finally, a 2D method referred to as MQ-J-HETCOR was reported [40], which correlated ^{27}Al and ^{31}P nuclei under the isotropic resolution offered by multiple quantum magic angle spinning (MQMAS) NMR [41]. Again, these 2D experiments did not require that the spectrally resolved J multiplets be directly observable.

In addition to the obvious benefit of providing a chemical-bond map between the spins, a potential advantage of using the INEPT and HMQC schemes in HETCOR spectroscopy is that they do not require spin locking. In the case of half-integer quadrupolar nuclei, the spin dynamics involved in both the spin locking and the CP processes are indeed very complicated under MAS, which may lead to lack of quantitative accuracy and low sensitivity [42–44]. Special care must be taken to find the best Hartmann–Hahn matching condition, which depends on several experimental parameters and can vary from site to site.

The J-HETCOR schemes, however, have a major drawback of their own in that the delays involved in the sequences are inversely proportional to the strength of the J_{SI} coupling constant between spins I and S [45]. Unless the homogeneous interactions can be sufficiently suppressed to facilitate the desired transfer of coherences, the non-refocusable transverse relaxation may force a substantial shortening of these delays and loss of efficiency. Additional difficulties may arise due to the complex nutation behavior of the quadrupolar spins in response to multi-pulse sequences. This behavior was analyzed in detail by Kao and Grey [7] for the case of an INEPT experiment on isolated spin pairs consisting of spin-1/2 (S) and half-integer quadrupolar ($I = 3/2$ or $5/2$) nuclei.

Herein, we use a similar formalism to describe the performance of refocused INEPT (R-INEPT) and HMQC experiments in the case of multi-spin systems SI_n ($n \leqslant 4$), where both S and I spins can be spin-1/2 or half-integer quadrupolar nuclei. The sensitivity and resolution offered by R-INEPT and HMQC are discussed in the context of high resolution experiments involving MQMAS and STMAS [46]. Finally, the theoretical analyses are verified by measuring the build-up of $^{31}P\{^{27}Al\}$ and $^{27}Al\{^{31}P\}$ magnetizations in R-INEPT and HMQC experiments under MAS in berlinite and the 2D HETCOR spectra of $AlPO_4$-14 aluminophosphate.

We chose to focus specifically on R-INEPT and HMQC for several reasons. The INEPT method, which was designed to improve the sensitivity of proton-attached carbon spectra in liquids [45], yields multiplets of vanishing integrated intensity due to their antiphase disposition. In order to obtain pure absorption spectra and enable using I-spin decoupling during observation, the alignment of multiplets can be achieved with R-INEPT by using an additional refocusing period [47–49]. The INEPT+ method has been proposed to reduce the phase and multiplet anomalies [50], whereas the DEPT sequence uses hetero-nuclear multiple quantum coherences during the polarization transfer [51]. This transfer is similar in all these methods, and works with comparable efficiency in liquid state NMR [50]. In solids, the aforementioned relaxation processes interfere with the polarization transfer. Overall, we found the R-INEPT alternative to be most sensitive and robust, at least in the applications involving ^{27}Al and ^{31}P, where it also compared favorably with cross polarization via dipolar interactions [40]. The HSQC [52] and HMQC [53] experiments are extensively used in liquids for studying single-bond hetero-nuclear shift correlations with indirect detection [52]. Although the correlation data provided by these two methods are essentially equivalent, HMQC uses considerably less pulses than HSQC, which benefits the applications involving quadrupolar nuclei.

2. Theory

We begin by considering the standard R-INEPT experiment, shown in Fig. 1a, involving an isolated pair of chemically bonded I and S nuclei. The signal intensity (build-up curve) observed in the S channel can be written as

$$s(t_1,t_2)_{\text{R-INEPT}} \approx \alpha \sin(\pi J_{SI}\tau)\sin(\pi J_{SI}\tau')\cos(2\pi\nu_I t_1), \qquad (1)$$

where $\alpha = \gamma_I\gamma_S^2\exp(i2\pi\nu_S t_2)$, J_{SI} is the scalar coupling, γ_I and γ_S are the nuclear magnetogyric ratios, while τ and τ' denote the delays used in the pulse sequence. In the HMQC experiment (Fig. 1c), the signal is observed with an intensity given by

$$s(t_1,t_2)_{\text{HMQC}} \approx \beta \sin^2(\pi J_{SI}\tau)\cos(2\pi\nu_I t_1), \qquad (2)$$

where $\beta = \gamma_S^3\exp(i2\pi\nu_S t_2)$. When the experiments are optimized, i.e., $\tau_{\text{opt}} = \tau'_{\text{opt}} = 1/2J_{SI}$, the relative sensitivity of these two experiments is in the order of $(\gamma_I/\gamma_S)^{3/2}$. For example, in the case of ^{1}H and ^{15}N, HMQC leads to a gain in S/N ratio of around 30 over R-INEPT.

In the following, these well-known results will be extended to include quadrupolar nuclei in isolated pairs (Sections 2.1.1, 2.1.2, 2.1.3 and 2.2.1, 2.2.2, and 2.2.3) and multi-spin

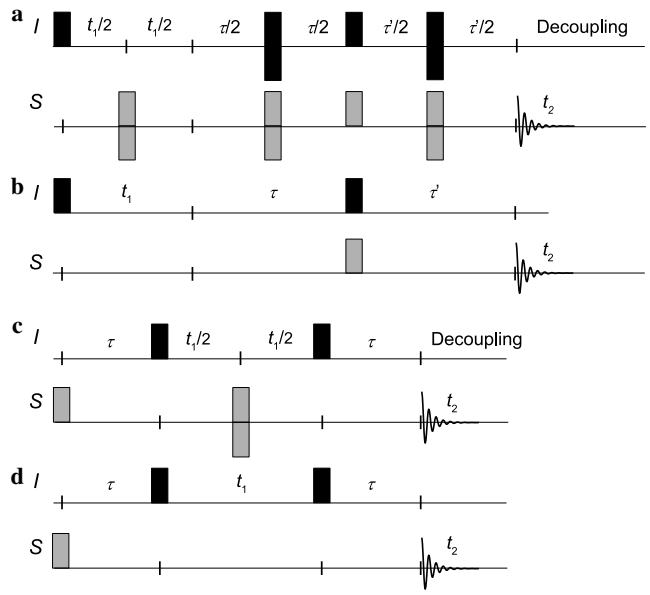

Fig. 1. (a), (c) R-INEPT and HMQC pulse sequences under MAS and the corresponding reduced static schemes used in the calculations (b and d).

systems (Sections 2.1.4 and 2.2.4). The analytical calculations were carried out using the spin operators that were first introduced by Vega to investigate the MAS spin-locking of quadrupolar nuclei [42,43]. The observed nucleus will be denoted S and the non-observed I. We will assume that the experiments are performed under MAS with rotor synchronization, i.e., $t_1/2$, $\tau/2$, and $\tau'/2$ in Fig. 1a, or $t_1/2$, and τ in Fig. 1c, are multiples of the rotor period $1/\nu_R$. This will allow us to treat the experiments theoretically as if they were performed in the static case while taking into account only the isotropic contributions from scalar (J_{II}, J_{SS}, J_{SI}), chemical shift (ν_{CS}), and quadrupole (ν_{QIS}) interactions. Rotor synchronization also eliminates the spinning sidebands from the spectrum along the F_1 dimension, while reducing its spectral-width to $\nu_R/2$. It may also facilitate the magnetization transfer from the outer levels of strongly quadrupolar nuclei [7]. We further assume that (i) the homo-nuclear dipolar interactions are eliminated either by MAS alone or with an additional adequate decoupling pulse sequence, i.e., the spin systems SI_n are always considered to be isolated, and (ii) the hetero-nuclear dipolar and J_{SI} dephasings are removed during acquisition of the FIDs.

The pulse lengths are considered to be negligibly short for spin-1/2 nuclei. For quadrupolar spins, the calculations will be performed separately for strong and weak quadrupole interactions. In the first case, the RF magnetic field ν_{RF} is always assumed to be smaller than the quadrupole coupling constant C_Q ($\nu_{RF} \ll C_Q$), such that only the central transition can be efficiently excited as a result of on-resonance excitation. The quadrupole coupling constant C_Q is defined as $C_Q = e^2qQ/h$, where eq is the largest principal axis value of the electric field gradient (EFG) tensor, eQ is the nuclear quadrupole moment, and h is the Planck constant. When C_Q is sufficiently small ($\nu_{RF} \gg C_Q$), the RF pulses excite the central transition (CT) and the satellite transitions (STs).

Only first-order quadrupole interactions (H_{Q1}) will be considered explicitly in the calculations, and irreversible transverse relaxation processes will be neglected in the time scale of our interest (J_{SI}^{-1}). For the observed S spins, we will assume the chemical shift anisotropy (CSA) is smaller than ν_R, i.e., only the first order quadrupole interactions can be responsible for the spinning sidebands in the F_2 dimension. Finally, it is assumed that the RF irradiation ν_{RF} is applied on resonance in all experiments. To simplify the equations, we introduce the following notation:

$$s_{pJ} = \sin(\pi p J_{SI}\tau),\ c_{pJ} = \cos(\pi p J_{SI}\tau),$$
$$s'_{pJ} = \sin(\pi p J_{SI}\tau'),\ c'_{pJ} = \cos(\pi p J_{SI}\tau') \quad (3)$$

2.1. R-INEPT MAS experiment

We refer again to the R-INEPT pulse sequence shown in Fig. 1a. An additional $\pi/2$ pulse, shifted by 90° with respect to the phase of the first pulse, can be added in the I channel at the end of evolution period to select a pure cosine or sine signal for the hyper-complex data treatment. The first π pulse at the S spin frequency refocuses the hetero-nuclear J_{SI} coupling during t_1. This pulse can be replaced by CW decoupling, in order to double the spectral range in the F_1 dimension (rotor synchronization can be applied to t_1 instead of $t_1/2$).

Dephasings related to chemical shift (ν^I_{CS}) and quadrupole induced shift (ν^I_{QIS}) during τ are refocused by the first π pulse at the I spin frequency, whereas those due to ν^S_{CS} and ν^S_{QIS} at the end of τ' are eliminated by the third π pulse applied to S spins. In the calculations we will also neglect dephasings related to homo-nuclear scalar couplings J_{II} during τ and J_{SS} during τ'. These scalar couplings may affect the intensity of the cross-peaks, but not their frequencies. Under these assumptions, the experiment can be reduced to the scheme shown in Fig. 1b, where the following frequencies are operable

$$I \text{ spins}: \frac{\pi}{2} \leftarrow t_1 : \nu_I \rightarrow\leftarrow \tau : J_{SI} \rightarrow \frac{\pi}{2}$$
$$\text{S spins}: \frac{\pi}{2} \leftarrow \tau' : J_{SI} \rightarrow\leftarrow t_2 : \nu_S \rightarrow,$$

with $\nu_I = J_{II} + \nu^I_{CS} + \nu^I_{QIS}$ and $\nu_S = J_{SS} + \nu^S_{CS} + \nu^S_{QIS}$. In the case when acquisition is not made in a rotor synchronized way, a term $p\nu_R$ with $p = 0, \pm1, \pm2, \ldots$, should be included in ν_S to account for the spinning sidebands. Decoupling of I spins during the acquisition cancels all anti-phase terms leading to a pure absorption signal.

2.1.1. I = k/2, S = 1/2

2.1.1.1 Let us first consider weak quadrupole interactions, where $\nu^I_{RF} \gg C^I_Q$. In this case, we can neglect the quadrupole induced shift, and in a rotor-synchronized experiment there is only a single frequency $\nu_I = J_{II} + \nu^I_{CS}$ associated

Table 1
Optimal values τ'_{opt}, in units of $1/J_{SI}$, and the corresponding maximum signal for $I = k/2$ (assuming a weak quadrupole interaction) and $S = 1/2$

I	1/2	3/2	5/2	7/2	9/2
τ'_{opt}	0.5	0.176	0.115	0.084	0.067
$s(0,0)_{max}/\gamma_I\gamma_S^2$	1	1.757	2.622	3.493	4.365

with all I spin transitions. The observed signal can be written as

$$s(t_1,t_2) \approx \alpha \frac{s_J}{I+1/2}\left(s'_J + 3s'_{3J} + \cdots + 2Is'_{2IJ}\right)\cos(2\pi\nu_I t_1) \quad (4)$$

In the 2D spectrum, each correlation peak is represented by multiplets centered at (ν^I_{CS}, ν^S_{CS}) and separated by J_{II} along F_1 and by J_{SS} along F_2. For $I = 1/2$, Eq. (4) is the same as Eq. (1). It is noted that (i) the maximum efficiency is always reached at $\tau_{opt} = 0.5/J_{SI}$ and (ii) the optimal second delay τ'_{opt} decreases and the maximum signal increases when the spin value I of the non-observed, weakly quadrupolar nucleus increases (see Table 1).

2.1.1.2 In the case of strong quadrupole interaction ($\nu^I_{RF} \ll C^I_Q$), only the CT is manipulated by RF irradiation (referred to as 'soft' pulse), while the STs are essentially unaffected and remain embedded in the background noise along F_1 dimension. Hence Eq. (4) becomes

$$s(t_1,t_2) \approx \alpha \frac{s_J s'_J}{I+1/2}\cos(2\pi\nu_I t_1) \quad (5)$$

The quadrupole induced shifts involved in ν_I are those of the CTs. Along F_1, one observes the CT MAS powder patterns corresponding to different sites, shifted every J_{II}. The maximum signal is scaled by $I + 1/2$ with respect to that given by Eq. (1), whereas the optimal delays remain unchanged, $\tau_{opt} = \tau'_{opt} = 0.5/J_{SI}$. The resulting R-INEPT spectra are not quantitative, even when the different spin pairs have the same J_{SI} coupling constants. Indeed, lets suppose that two ^{31}P(–O–)^{27}Al pairs are observed with the same scalar couplings but different quadrupole interactions. For $\tau_{opt} = 0.5/J_{SI}$, the observed ^{31}P magnetizations depend on the size of the ^{27}Al quadrupole interaction:

$$\text{small } C_Q(\nu^I_{RF} \gg C^I_Q) : \tau'_{opt} \approx 0.115/J_{SI}, s(0,0)_{opt} = 2.622\gamma_I\gamma_S^2$$

$$\text{large } C_Q(\nu^I_{RF} \ll C^I_Q) : \tau'_{opt} \approx 0.5/J_{SI}, s(0,0)_{opt} = 0.333\gamma_I\gamma_S^2$$

The latter signal becomes further reduced when the second-order quadrupole interactions (H_{Q2}) are taken into consideration in the calculations.

2.1.2. I = 1/2 and S = h/2

In this case, one may observe separately several transitions, whose behavior must be analyzed individually.

2.1.2.1 Again, we initially consider the case of weak quadrupole interactions, when the quadrupole induced shifts are negligibly small and all transitions yield the same observable frequencies.

2.1.2.1.1 Since the quadrupolar nuclei are being observed in the F_2 dimension, we will include in the discussion the experiments performed without rotor synchronized acquisition. In such case, the observed frequencies can be written as $\nu_S = J_{SS} + \nu^S_{CS} + p\nu_R$. When the sample spinning rate is sufficiently slow ($\nu^S_{RF} \gg C^S_Q > \nu_R$), several families of spinning sidebands are observable along F_2 for every site. Each family is symmetrical with respect to the center-band (we ignore here the CSA) and is the sum of overlapping individual patterns corresponding to the CT and all pairs of symmetric ST_q transitions ($q = 1, \ldots, S - 1/2$). These patterns are further affected by J_{SS}. During τ, the Zeeman states ($m = \pm 1/2, \ldots, \pm S/2$) which influence the J_{SI} coupling are associated with the quadrupolar S spins, which leads to an evolution described by $A_1 s_J + \cdots + A_{2m} s_{2mJ} + \cdots + A_{2S} s_{2SJ}$. During τ', only the $\pm 1/2$ Zeeman states of spin $I = 1/2$ are involved, which leads to a sole s'_J term with $\tau'_{opt} = 0.5/J_{SI}$. The intensity of individual sideband patterns associated with the CT or with pairs of symmetrical ST_q's can thus be written

$$s(t_1,t_2) \approx \alpha \frac{3B}{2^{2S-1}S(S+1)(2S+1)}(A_1 s_J + A_3 s_{3J} + \cdots + A_{2S} s_{2SJ}) s'_J \cos(2\pi\nu_I t_1) \quad (6)$$

with coefficients B, describing the CT or ST_q pattern, and A_{2m}, describing the Zeeman states with $m = 1/2, \ldots, S$, as given in Table 2.

2.1.2.1.2 In the experiments performed with rotor synchronized acquisition (or in the liquid state), resonances corresponding to CT and ST_q pairs appear at the same frequency $\nu_S = J_{SS} + \nu^S_{CS}$. The observed signal can be calculated as a sum of all A_{2m} terms in Table 2, weighted by their corresponding B values

Table 2
Values of parameter B and A_{2m} in Eq. (6) as a function of S, for the central and satellite transitions

S	Transition	B	A_1	A_3	A_5	A_7	A_9
1/2	CT	1	1/2				
3/2	CT	1	1	−3			
	ST_1	−3	1	1			
5/2	CT	3	−2	1	−5		
	ST_1	4	2	−3	−5		
	ST_2	−5	2	3	1		
7/2	CT	2	9	−15	5	−35	
	ST_1	15	−3	1	−3	−7	
	ST_2	6	5	−3	−15	−7	
	ST_3	−7	5	9	5	1	
9/2	CT	5	−18	12	−28	7	−63
	ST_1	24	6	−8	0	−7	−21
	ST_2	−84	2	0	0	5	3
	ST_3	8	14	0	−40	−35	−9
	ST_4	−9	14	28	20	7	1

Table 3
Optimal values, in units of $1/J_{SI}$, and the corresponding maximum R-INEPT signal for $I = 1/2$ and $S = h/2$ in the case of weak quadrupole interaction

S	1/2	3/2	5/2	7/2	9/2
$\tau_{opt}(1/J_{SI})$	0.5	0.176	0.115	0.084	0.067
$s(0,0)_{max}/\gamma_I\gamma_S^2$	1.0	0.3511	0.2248	0.1663	0.1323

$$s(t_1,t_2) \approx \alpha \frac{3}{2S(S+1)(2S+1)}(s_J + 3s_{3J} + \cdots + 2Ss_{2SJ})s'_J \times \cos(2\pi\nu_I t_1). \quad (7)$$

The maximum signal is always observed at $\tau'_{opt} = 0.5/J_{SI}$, but with a shorter first delay τ_{opt}, as shown in Table 3. It is also less intense than in the case of $I = S = 1/2$ (see Eq. (1)), in agreement with the results obtained for the INEPT experiments in solution-state NMR [49,54,55]. This result is analogous to that obtained for $I = k/2$, $S = 1/2$ [Eq. (4)], with switched over delays τ and τ'.

2.1.2.2 In the case of strong quadrupole interactions, we again bear in mind that only the central transition is observable under 'soft' RF pulses at the frequency of the S spin. The resulting signal is the same as given by Eq. (1), assuming that the powder-averaged intensity observed after a CT-selective 90° pulse is normalized to unity. Along the F_2 dimension, an MAS-narrowed CT powder pattern is observed, whose intensity evolution as a function of τ and τ' is identical to that observed for $I = S = 1/2$. This pattern can be further affected by J_{SS}.

2.1.3. I = k/2 and S = h/2

Once more, we limit our analysis to rotor-synchronized experiments and two extreme cases of weak or strong quadrupole interactions, for which the previous results can be easily generalized. In the case of liquid-state samples or weak quadrupole interactions with rotor-synchronized data acquisition, one obtains $\nu_I = J_{II} + \nu^I_{CS}$, $\nu_S = J_{SS} + \nu^S_{CS}$ and

$$s(t_1,t_2) \approx \alpha \frac{3}{(2I+1)S(S+1)(2S+1)} \times (s_J + 3s_{3J} + \cdots + 2Ss_{2SJ}) \times \left(s'_J + 3s'_{3J} + \cdots + 2Is'_{2IJ}\right)\cos(2\pi\nu_I t_1) \quad (8)$$

In the case of strong quadrupole interactions, only the central transitions in I and S spins are observable, and one must use the CT-selective pulses in order to correctly manipulate their density matrices. The resulting CT signal of S spins is again given by Eq. (5), if we assume that the powder-averaged intensity observed after a CT-selective 90° pulse at the S spins frequency is normalized to 1. As expected, the signal evolution is similar to that of a spin-1/2 pair [Eq. (1)], with an amplitude scaled by $(I+1/2)^{-1}$.

2.1.4. Multi-spin system: SI_n

2.1.4.1 Let us first consider the simplest case of $I = S = 1/2$. For identical scalar couplings and $n \leqslant 3$, the formulae are well known [47] and often used for separating the multiplets. However, in three dimensional solid-state networks, the individual J couplings within the SI_n ($n > 3$) spin systems can be considerably different [56]. In such general case, the in-phase 2D signal can be written

$$\begin{aligned}
SI: &\quad s(t_1,t_2) \approx \alpha s_J s'_J \cos(2\pi\nu_I t_1)\\
SI_2: &\quad s(t_1,t_2) \approx \alpha[s_{J1}s'_{J1}c'_{J2}\cos(2\pi\nu_{I1}t_1) + s_{J2}s'_{J2}c'_{J1}\cos(2\pi\nu_{I2}t_1)]\\
SI_3: &\quad s(t_1,t_2) \approx \alpha[s_{J1}s'_{J1}c'_{J2}c'_{J3}\cos(2\pi\nu_{I1}t_1) + s_{J2}s'_{J2}c'_{J1}c'_{J3}\cos(2\pi\nu_{I2}t_1) + s_{J3}s'_{J3}c'_{J1}c'_{J2}\cos(2\pi\nu_{I3}t_1)]\\
SI_4: &\quad s(t_1,t_2) \approx \alpha[s_{J1}s'_{J1}c'_{J2}c'_{J3}c'_{J4}\cos(2\pi\nu_{I1}t_1) + s_{J2}s'_{J2}c'_{J1}c'_{J3}c'_{J4}\cos(2\pi\nu_{I2}t_1) + s_{J3}s'_{J3}c'_{J1}c'_{J2}c'_{J4}\cos(2\pi\nu_{I3}t_1) + s_{J4}s'_{J4}c'_{J1}c'_{J2}c'_{J3}\cos(2\pi\nu_{I4}t_1)]
\end{aligned} \quad (9)$$

When all J-couplings are equal, the maximum 1D signal representing an SI_n spin system is always observed for $\tau_{opt} = 0.5/J_{SI}$ with the intensity given by

$$s(t_1 = 0, t_2) \approx \alpha n s_J s'_J (c'_J)^{n-1} \quad (10)$$

The value of τ'_{opt} depends on n, and is observed for $J_{SI}\tau'_{opt}$ equal to 0.5 ($n = 1$), 0.25 ($n = 2$), 0.19 ($n = 3$) and 0.167 ($n = 4$) with $s(0,0)_{max}/\gamma_I\gamma_S^2 = 1, 1, 1.15$ and 1.3, respectively. An average value of $\tau' = 1/3J_{CH}$ is often recommended in solution NMR studies involving e.g., ^{1}H–^{13}C R-INEPT experiments. Indeed, for CH, CH_2 and CH_3 it yields the relative intensities $s(0,0)_{max}/\gamma_H\gamma_C^2$ of 0.87, 0.87 and 0.65, respectively.

2.1.4.2 The above results can be easily generalized to SI_n systems consisting of half-integer quadrupolar nuclei. For example, in the case of two such nuclei submitted to strong quadrupole interactions, one has to apply CT-selective pulses at both frequencies, which results in the same S spins evolution as for SI_n systems of spin-1/2 nuclei [Eq. (9)] scaled by $I + 1/2$:

$$\begin{aligned}
SI: &\quad s(t_1,t_2) \approx \alpha \frac{s_J s'_J}{I+1/2}\cos(2\pi\nu_I t_1)\\
SI_2: &\quad s(t_1,t_2) \approx \alpha \frac{1}{I+1/2}[s_{J1}s'_{J1}c'_{J2}\cos(2\pi\nu_{I1}t_1) + s_{J2}s'_{J2}c'_{J1}\cos(2\pi\nu_{I2}t_1)]
\end{aligned} \quad (11)$$

The CT powder patterns, narrowed by MAS and affected by J_{II} and J_{SS}, are observed in F_1 and F_2 dimensions of the 2D spectra.

2.2. HMQC MAS experiment

The basic HMQC pulse sequence is shown in Fig. 1c. The dephasing due to J_{SI} during t_1 is cancelled by the

π pulse in the S channel, while that related to $J_{SS} + \nu^S_{CS} + \nu^S_{QIS}$ at the $+1Q$ level are negated by the subsequent evolution at the $-1Q$ level. As in the case of R-INEPT, the experiment can be reduced to the sequence shown in Fig. 1d, with the following terms governing the evolution of magnetization:

$$I \text{ spins} : \frac{\pi}{2} \leftarrow t_1 : \nu_I \rightarrow \frac{\pi}{2}$$
$$S \text{ spins} : \frac{\pi}{2} \leftarrow \tau : J_{SI} \rightarrow\leftarrow \; t_1 \; \rightarrow\leftarrow \tau : J_{SI} \rightarrow t_2 : \nu_S,$$

where $\nu_I = J_{II} + \nu^I_{CS} + \nu^I_{QIS}$ and $\nu_S = J_{SS} + \nu^S_{CS} + \nu^S_{QIS}$. The term $p\nu_R$ may be included during t_2 if the acquisition is not synchronized with the rotor. Again, we will consider the isolated spin pairs (Sections 2.2.1, 2.2.2, and 2.2.3) and multi-spin systems (Section 2.2.4).

2.2.1. I = k/2, S = 1/2

When the quadrupole interaction is weak or the sample is studied in solution, the signal is similar to that observed for a pair of spin-1/2 nuclei [Eq. (2)]. Since the quadrupole induced shifts are negligible, the observed cross-peak multiplets are centered at (ν^I_{CS}, ν^S_{CS}) and separated by J_{II} in F_1 and J_{SS} in F_2.

When the quadrupole interaction is large, only the central transition is observable and both $\pi/2$ pulses in the I channel should be CT-selective in order to correctly manipulate the spin density matrix. The observed signal

$$s(t_1, t_2) \approx \beta \frac{s_J^2}{I + 1/2} \cos(2\pi\nu_I t_1), \tag{12}$$

is decreased by a factor $I + 1/2$ with respect to spin-1/2 nuclei. The quadrupole induced shifts involved in ν_I are those of the CTs. Along F_1, the CT MAS powder patterns are observed, shifted by J_{II}.

2.2.2. I = 1/2 and S = h/2

In liquid-state NMR, all transitions have the same resonance frequency $\nu_S = J_{SS} + \nu^S_{CS}$, and the build-up curves exhibit the same behavior as for a spin-1/2 pairs [Eq. (2)].

In the case of weak quadrupole interactions in solids, each transition of the S spin behaves as spin-1/2. If the data acquisition is rotor-synchronized, all sidebands are aliased onto the center-band, and the spectrum is identical to that observed in solutions with HMQC. In the case of non-synchronized acquisition, the observed powder spectra are analogous to the spinning sideband pattern observed after a hard $\pi/2$ pulse at the S spin frequency, but scaled down in intensity by a factor of s_J^2 ($\tau_{opt} = 0.5/J_{SI}$).

In the case of large quadrupole interaction, a CT-selective excitation must be used, and the signal amplitude is scaled by s_J^2 with regard to that observed after a selective $\pi/2$ pulse.

2.2.3. I = k/2 and S = h/2

The previous results can be easily generalized to spin pairs consisting of two half-integer quadrupolar nuclei. If both quadrupole interactions are weak, the signal intensity is identical to that given in Eq. (2) for $I = S = 1/2$. The resulting cross-peaks appear as multiplets centred at (ν^I_{CS}, ν^S_{CS}) and separated by J_{II} along F_1 and J_{SS} along F_2. When both quadrupole interactions are strong, the CT-selective pulses should be used in the I and S channels. The resulting evolution of magnetization is similar to that of a spin-1/2 pair, but the observed amplitude is reduced by $I + 1/2$ with respect to that observed after a selective 90° pulse in the S channel.

2.2.4. Multi-spin system: SI_n

The standard HMQC experiment utilizes two phases in the I channel in order to select $\pm 1Q$ coherence levels during t_1. In the case of an SI_2 spin system, the signal is equal to

$$s(t_1, t_2) \approx -\beta[s_{J1}^2 c_{J2}^2 \cos(2\pi\nu_{I1} t_1) + s_{J2}^2 c_{J1}^2 \cos(2\pi\nu_{I2} t_1)] \tag{13}$$

When $n = 3$ or 4, a small contribution due to the $\pm 3Q$ levels is selected during t_1 at the sum of three I resonance frequencies involved, unless a more restrictive phase cycling is used. Recently, it has been demonstrated that appropriate MQ filtering during t_1 can lead to unambiguous spectral editing [15]. For example, a clear distinction between CH_2 and CH_3 groups has been achieved by comparing $2Q$- and $3Q$-filtered HMQC spectra.

The multiple-quantum intensities observed for an SI_n system of spin-1/2 nuclei submitted to identical J couplings are as follows (also, see Appendix A):

$$\begin{aligned}
SI: \quad & s(0,t_2) \approx \beta[c_J^2(0Q) - s_J^2(\pm 1Q)] \\
SI_2: \quad & s(0,t_2) \approx \beta[(c_J^4 + 0.5 s_J^4)(0Q) \\
& \quad - 2 s_J^2 c_J^2(\pm 1Q) + 0.5 s_J^4(\pm 2Q)] \\
SI_3: \quad & s(0,t_2) \approx \beta[(c_J^6 + 1.5 s_J^4 c_J^2)(0Q) \\
& \quad - (3 s_J^2 c_J^4 + 0.75 s_J^6)(\pm 1Q) \\
& \quad + 1.5 s_J^4 c_J^2(\pm 2Q) - 0.25 s_J^6(\pm 3Q)] \\
SI_4: \quad & s(0,t_2) \approx \beta[(c_J^8 + 3 s_J^4 c_J^4 + 0.375 s_J^8)(0Q) \\
& \quad - (4 s_J^2 c_J^6 + 3 s_J^6 c_J^2)(\pm 1Q) \\
& \quad + (3 s_J^4 c_J^4 + 0.5 s_J^8)(\pm 2Q) \\
& \quad - s_J^6 c_J^2(\pm 3Q) + 0.125 s_J^8(\pm 4Q)],
\end{aligned} \tag{14}$$

where in parenthesis we have indicated the level of coherence responsible for a given contribution. The total signal from all I quantum levels in a SI_n multi-spin system is equal to that observed in the J-RES experiment [11], which does not use any phase cycling in the I channel

$$s(0, t_2) \approx \beta \cos^n(2\pi J_{SI}\tau) \tag{15}$$

The relative values of total intensity expected in R-INEPT and HMQC experiments in SI_n spin systems with identical J_{SI} scalar couplings, are listed in Table 4. Both methods have approximately the same efficiencies when $n = 1$, 3. As expected, the $\pm 3Q$ and $\pm 4Q$ filtering reduces the observed HMQC signal.

In the 2D experiments with a multiple-quantum filtering, cross-peaks observed along F_1 are combinations of

Table 4
Total intensity (I_{tot}) observed in SI_n spin systems with identical J_{SI} scalar couplings, calculated using Eq. (9) for R-INEPT ($\tau_{opt} = 0.5/J_{SI}$) and using Eq. (14) for HMQC

n	R-INEPT τ'_{opt}	R-INEPT I_{tot}	HMQC ±1,±3Q τ_{opt}	HMQC ±1,±3Q I_{tot}	HMQC ±2Q τ_{opt}	HMQC ±2Q I_{tot}	HMQC ±3Q τ_{opt}	HMQC ±3Q I_{tot}	HMQC ±4Q τ_{opt}	HMQC ±4Q I_{tot}
1	0.500	1	0.50	−1						
2	0.250	1	0.25	−0.5	0.50	0.5				
3	0.200	1.154	0.50	−1	0.31	0.222	0.50	−0.25		
4	0.167	1.3	0.25	−0.5	0.50	0.5	0.33	−0.105	0.5	0.125

All magnetogyric ratios are assumed to be equal to 1 and the optimum delays are given in units of $1/J_{SI}$. In a 2D experiment, the intensity corresponding to each I resonance should be divided by n if I spins resonate at different frequencies. In the case of HMQC with ±1Q selection for I spins, we took into account the interference from ±3Q levels.

the frequencies of the I species. For example, in the case of an SI_2 spin-system with different resonance frequencies (ν_{I1}, ν_{I2}) and scalar couplings (J_1, J_2), the signal is a sum of contributions from 0Q, ±1Q and ±2Q coherences

$$\begin{aligned} s(t_1,t_2) \approx{}& \beta\{c_{J1}^2 c_{J2}^2 + 0.5 s_{J1}^2 s_{J2}^2 \cos[2\pi(\nu_{I1}-\nu_{I2})t_1]\}(0Q) \\ & - \beta[s_{J1}^2 c_{J2}^2 \cos(2\pi\nu_{I1}t_1) + s_{J2}^2 c_{J1}^2 \cos(2\pi\nu_{I2}t_1)](\pm 1Q) \\ & + \beta\{0.5 s_{J1}^2 s_{J2}^2 \cos[2\pi(\nu_{I1}+\nu_{I2})t_1]\}(\pm 2Q) \end{aligned} \quad (16)$$

Formulae for other spin systems are given in Appendix A

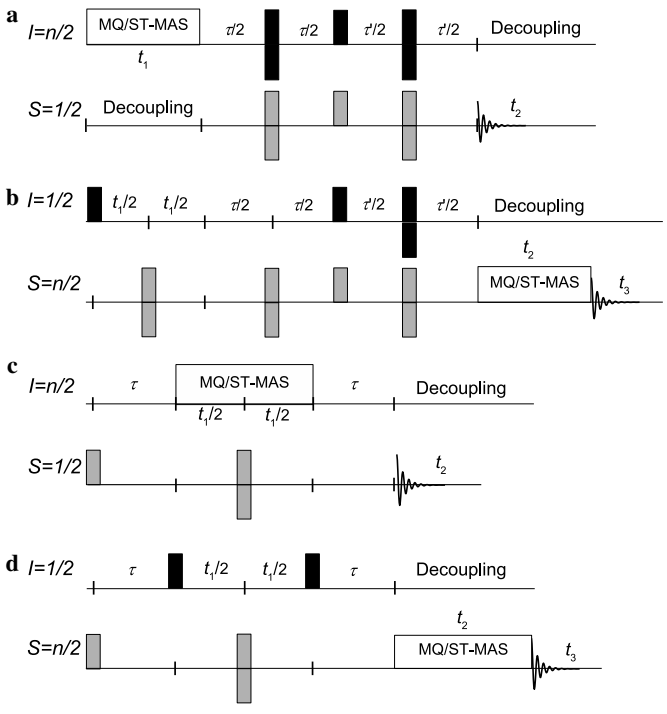

Fig. 2. (a), (b) High-resolution J-HETCOR sequences based on polarization transfer via R-INEPT, which use the quadrupolar (a) or spin-1/2 (b) nuclei as the initial source of polarization. Sequence (a) leads to a 2D spectrum featuring the isotropic shift δ_{iso} in the F_1 dimension and the chemical shift δ_{CS} in the F_2 dimension. F_1 and F_2 dimensions are reversed in 3D experiment (b), and F_3 corresponds to the quadrupolar MAS spectrum. The equivalent HMQC sequences are shown in figures (c) and (d). Sequence (c) leads to a 2D spectrum featuring the isotropic shift δ_{iso} in the F_1 dimension and the chemical shift δ_{CS} in the F_2 dimension. F_1 and F_2 dimensions are reversed in 3D experiment (d), and F_3 corresponds to the quadrupolar MAS spectrum.

2.2.5. High-resolution J-HETCOR experiments involving quadrupolar nuclei

We have previously described the R-INEPT and HMQC sequences performed under MAS. The J-HETCOR experiments can be also performed using MQMAS- or STMAS-based schemes in order to improve the resolution. Several experimental schemes involving direct observation of spin-1/2 or quadrupolar nuclei are depicted in Fig. 2. In the case of R-INEPT experiments, the preferred method, shown in Fig. 2a, uses the isotropic echo formed in the MQMAS (or STMAS) experiment at time t_1 as a source of polarization for spin-1/2 nuclei, as previously reported [40]. The MQMAS/STMAS period can be also introduced at the end of the sequence, as shown in Fig. 2b. The advantage of the first approach is that the measurement remains two-dimensional and can be repeated with the recycle delay controlled by the quadrupolar spins that usually relax faster. In both sequences, an additional π/2 pulse can be added in the I channel to "purge" the signal for hyper-complex treatment (as in Fig. 1a), either at the top of the isotropic echo (Fig. 2a), or at the end of the t_1 period (Fig. 2b). Hetero-nuclear decoupling can be used during t_1 and/or t_2, if needed [40].

Similar choices exist for the strategies involving the HMQC method (see Figs. 2c and d). Again, when the MQMAS or STMAS period constitutes t_1 (Fig. 2c), the experiment remains two-dimensional. The π pulse that is applied to the S spins in the middle of t_1 cancels dephasings due to $J_{SS} + \nu_{CS}^S + \nu_{QIS}^S$. Note, however, that this pulse does not fully refocus the dephasing due to J_{SI}.

3. Experimental

The experiments were performed on two aluminophosphates, berlinite and $AlPO_4$-14. The magnetization build-up curves characteristic of R-INEPT and HMQC methods (Section 3.1) were measured for berlinite on a Bruker Avance DSX-400 spectrometer using a 4 mm triple-resonance MAS probe. The same spectrometer and a Bruker Avance DSX-800 system, equipped with a 3.2 mm triple-resonance MAS probe, were used to obtain 2D ^{27}Al–^{31}P HETCOR spectra of $AlPO_4$-14 (Section 3.2). The experimental parameters are detailed in the figure captions.

In addition to the theoretical considerations described in Section 2, several practical concerns should be acknowledged. The correct manipulation of the density matrix of quadrupolar nuclei requires using weak CT selective pulses, whose lengths must be taken into account in rotor-synchronized pulse sequences. In the presence of resonance offsets, these pulses will not produce exact π or π/2 nutation for all spins, which may cause an additional loss of signal. In MAS-based experiments which use quadrupolar nuclei as the initial source of polarization (I spins in Fig. 1a or S spins in Fig. 1c), the S/N ratio can be enhanced by rotor assisted population transfer [57,58], fast amplitude modulation [59], double frequency sweeps [60] or hyperbolic secant pulses [61]. When S spins are quadrupolar, the spin-temperature inversion method should be used in order to eliminate unwanted signals. Finally, the acquisition of multiple echoes can be considered in samples with sufficiently long transverse relaxation [62,63].

3.1. Magnetization build-up curves for HMQC and R-INEPT

The crystallographic structure of berlinite (space group $P3_121$) involves one aluminum, one phosphorus, and two inequivalent oxygen sites [64]. Aluminum and phosphorus occupy tetrahedrally coordinated positions, Al–$(OP)_4$ and P–$(OAl)_4$, cross-linked by μ_2 bridging oxygens. The ^{31}P MAS signal consists of a single Gaussian line ($\delta_{CS} = -24.6$ ppm), and the ^{27}Al MAS signal shows a typical second order quadrupolar line shape ($\delta_{CS} = 42.9$ ppm, $C_Q = 4.07$ MHz, and $\eta_Q = 0.34$) [65]. $J_{Al–O–P}$ scalar couplings are too weak (15–30 Hz) to be directly detected in the ^{27}Al or ^{31}P spectra.

Given the presence of two different oxygen sites, the ^{27}Al–^{31}P spin system of the berlinite 3D network can be approximated as SI_4 with two different scalar couplings and a single resonance frequency for ^{27}Al and ^{31}P. In such case, the HMQC signal amplitude, with $\pm 1Q$ and $\pm 3Q$ filtering, follows from Eq. (A4)

$$s(0,0) \approx -2\gamma_S^3(s_{J1}^2 c_{J2}^2 + s_{J2}^2 c_{J1}^2)(s_{J1}^2 s_{J2}^2 + c_{J1}^2 c_{J2}^2) \times \exp(-2\tau/T'_{2S}), \quad (17)$$

where T'_{2S} is the non-refocusable transverse relaxation time of the observed nuclei, which we neglected in our theoretical treatment. For a given sample, the transverse relaxation may depend on the coherences used, the spinning rate, and the decoupling schemes. When $J_1 = J_2$, Eq. (17) yields

$$s(0,0) \approx -\gamma_S^3 s_{2J}^2 (s_J^4 + c_J^4) \exp(-2\tau/T'_{2S}) \quad (18)$$

i.e., the signal approaches zero at $\tau = 1/2J$, and increases again without changing sign. Two experimental build-up curves, representing the initial intensities $s(0,0)$ in ^{27}Al{^{31}P} and ^{31}P{^{27}Al} HMQC experiments are shown in Figs. 3a and b. We have used two-phase cycling for I spins, which selected simultaneously their $\pm 1Q$ and $\pm 3Q$ levels [see Eqs. (14) and (A4)]. Under the conditions used

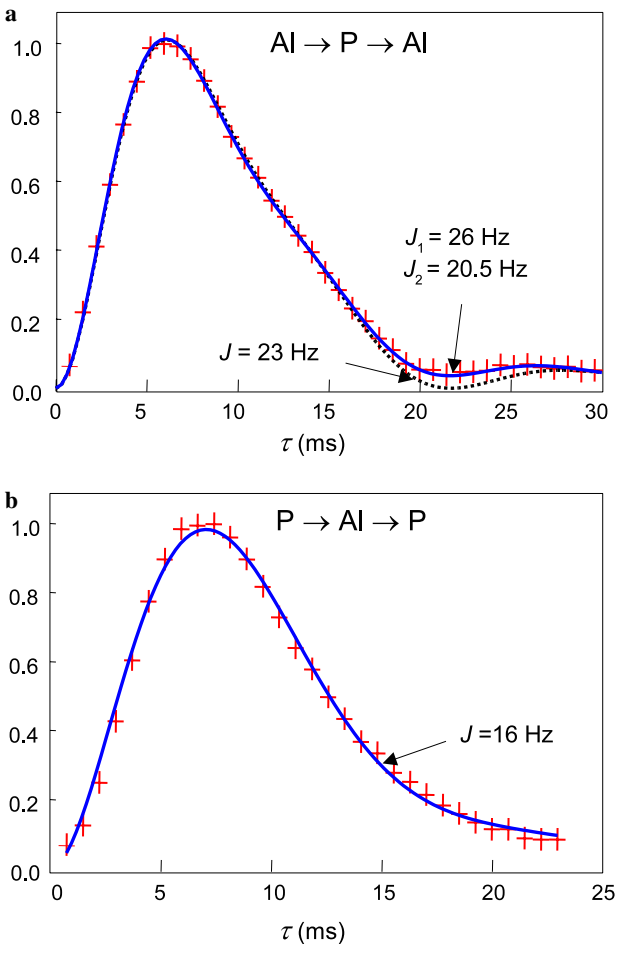

Fig. 3. HMQC build-up curves versus delay τ in berlinite with ^{27}Al (a) or ^{31}P (b) detection. The measurements (+) were performed at 9.4 T under the following conditions: $\nu_R = 13.5$ kHz, $\nu_{RF}^P = 60$ kHz and $\nu_{RF}^{Al} = 5$ kHz. The dotted curve in figure (a) shows the best fit obtained using Eq. (18) for $J = 23 \pm 1$ Hz and $T'_{2Al} = 15$ ms. Eq. (17) yielded $J_1 = 26 \pm 1$ Hz, $J_2 = 20.5 \pm 1$ Hz and $T'_{2Al} = 15$ ms (continuous curve). The data in figure (b) were fitted using Eq. (18) with $J = 16 \pm 2$ Hz and $T'_{2P} = 12 \pm 3$ ms.

in our experiments (see caption to Fig. 3), we have obtained the non-refocusable transverse relaxation times of $T'_{2Al} = 15 \pm 1$ ms and $T'_{2P} = 14 \pm 2$ ms. With the transverse relaxation times being similar for ^{27}Al and ^{31}P, the corresponding build-up curves reached their first maxima and minima at the same delay times $\tau_{max} \approx 6$ and $\tau_{min} \approx 22$–24 ms, respectively (see Fig. 3).

The best fit of experimental ^{27}Al{^{31}P} data which could be obtained using Eq. (18) gave $J = 23 \pm 1$ Hz (dotted curve in Fig. 3a). A better fit was obtained using Eq. (17), which yielded $J_1 = 26 \pm 1$ Hz and $J_2 = 20.5 \pm 1$ Hz (see Fig. 3a, continuous curve). The same two values were earlier inferred based on line-shape simulations of the ^{27}Al{^{31}P} J-HMQC spectrum [36]. For the ^{31}P{^{27}Al} build-up curve, slow longitudinal relaxation of ^{31}P nuclei ($T_1 \approx 1000$ s) resulted in poor S/N ratio and degraded the accuracy of the fits. Therefore, the distinction between J_1 and J_2 could not be made in this case. The fit based on Eq. (18) yielded $J = 16 \pm 2$ Hz and $T'_{2P} = 12 \pm 3$ ms (see Fig. 3b). These two fitted values are not accurate, due to

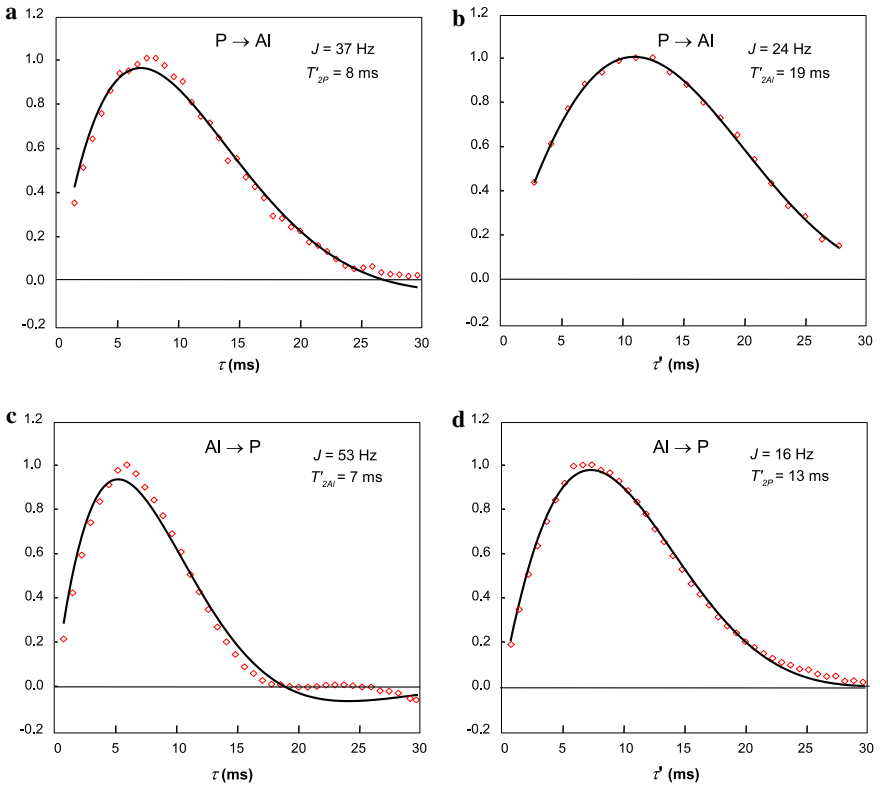

Fig. 4. R-INEPT build-up curve in berlinite with ^{27}Al observation versus delays τ (a) and τ' (b), and the corresponding results obtained with ^{31}P observation (c and d). The fixed delays were always adjusted to 8 ms. Other experimental conditions were the same as in Fig. 3. The data were fitted using Eq. (20), which yielded $J = 37 \pm 5$ Hz and $T'_{2P} = 8 \pm 4$ ms; $J = 24 \pm 2$ Hz and $T'_{2Al} = 19 \pm 2$ ms; $J = 53 \pm 6$ Hz and $T'_{2Al} = 7 \pm 4$ ms; $J = 16 \pm 3$ Hz and $T'_{2P} = 13 \pm 3$ ms, for figures (a), (b), (c) and (d), respectively.

the limited accessible τ range (22 ms) and the low signal intensity.

The build-up curves for ^{27}Al{^{31}P} and ^{31}P{^{27}Al} R-INEPT experiments on berlinite are plotted as a function of time delays τ and τ' in Fig. 4. For an SI_4 spin system with two different scalar couplings, Eq. (9) leads to

$$s(0,0) \approx 2\gamma_I\gamma_S^2 c'_{J1}c'_{J2}(s_{J1}s'_{J1}c'_{J2} + s_{J2}s'_{J2}c'_{J1}) \times \exp(-\frac{\tau}{T'_{2I}} - \frac{\tau'}{T'_{2S}}), \quad (19)$$

which for $J_1 = J_2 = J$ becomes

$$s(0,0) \approx 2\gamma_I\gamma_S^2 s_J s'_{2J}(c'_J)^2 \exp(-\frac{\tau}{T'_{2I}} - \frac{\tau'}{T'_{2S}}). \quad (20)$$

Again, the transverse relaxation terms were now reinstated in the equations, because they play a significant role in these measurements. According to Eq. (20), the signal should change sign at $\tau = 1/J \approx 44$ ms in Figs. 4a and c, or at $\tau' = 1/2J \approx 22$ ms in Figs. 4b and d. However, the build-up curves recorded as a function of τ and τ' are quite similar. Indeed, when fitted using Eq. (20), the build-up curves of Figs. 4b and d yield J and T'_2 values which are consistent with the previous estimates, as indicated in the figure caption. On the contrary, the evolution versus τ (Figs. 4a and c) generated inaccurate J and T'_2 values. Clearly, the attenuation of build-up curves due to transverse relaxation considerably reduces the quality of the fits. The second-order quadrupole interaction, which was not taken into account in our analytical calculations, is another source of this discrepancy. Indeed, numerical simulations performed with PULSAR [62] for an isolated spin-pair showed that second-order quadrupole interaction may decrease the signal and attenuate the built-up curves, especially when $\nu_{RF} \ll C_Q$. This effect is more significant in R-INEPT than in HMQC. Unfortunately, due to the very large size of the density matrix (2592×2592), these second-order effects can not be simulated under MAS for the SI_4 spin system. Another possible, albeit untested, scenario involves dephasing due to residual homo-nuclear dipolar or scalar interactions, which were unaccounted for in our simulations. It should be noted, however, that the simulations by PULSAR excluded the possibility of any contributions from through space (dipolar) polarization transfer between different nuclei in the studied sequences under rotor synchronized conditions.

3.2. 2D ^{27}Al–^{31}P HETCOR spectra of $AlPO_4$-14

$AlPO_4$-14 is a well-studied aluminophosphate [34,67–69], whose structure consists of a three-dimensional channel system formed by 8-ring pores with four different aluminum sites and four different phosphorus sites. Aluminum sites resonating at higher frequency (Al_2 and

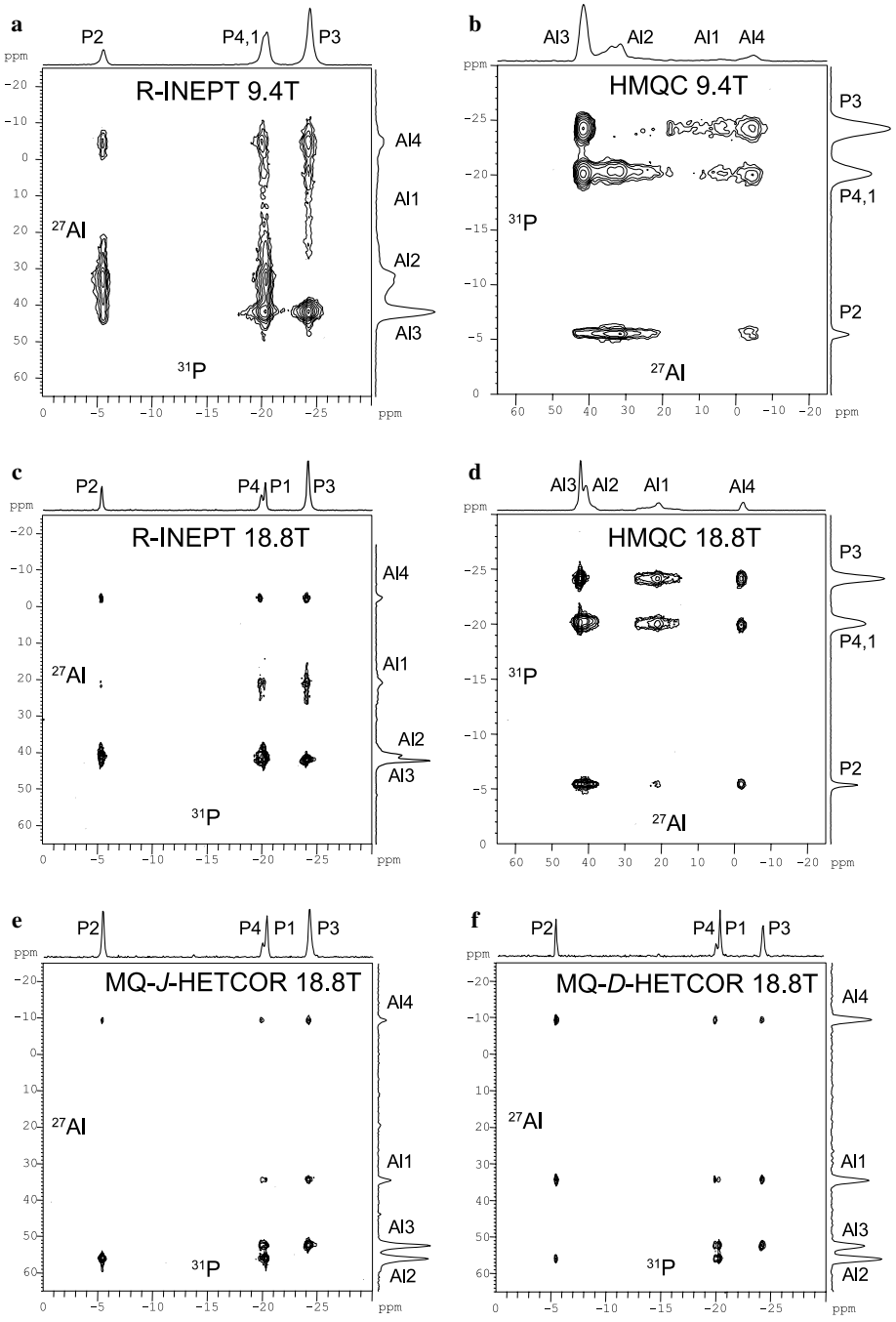

Fig. 5. 2D HETCOR spectra of $AlPO_4$-14: (a) $^{31}P\{^{27}Al\}$ R-INEPT at 9.4 T, (b) $^{27}Al\{^{31}P\}$ HMQC at 9.4 T, (c) $^{31}P\{^{27}Al\}$ R-INEPT at 18.8 T, (d) $^{27}Al\{^{31}P\}$ HMQC at 18.8 T, (e) $^{31}P\{^{27}Al\}$ SPAM-MQ-*J*-HETCOR with R-INEPT at 18.8 T, and (f) $^{31}P\{^{27}Al\}$ SPAM-MQ-*D*-HETCOR obtained using cross-polarization at 18.8 T. The total experimental times were 5 (a), 5 (b), 2 (c), 2 (d), 10 (e) and 7 (f) hours.

Al_3 with C_Q values of 4.1 and 1.8 MHz) have a tetrahedral structure, whereas Al_1 ($C_Q = 5.6$ MHz) and Al_4 ($C_Q = 2.6$ MHz) are five- and six-coordinated, respectively [34,68,69]. Similarly, four different phosphorus sites were observed under double-resonance decoupling at the ^1H and ^{27}Al spin frequencies [69], labeled as P_1 (at −20.6 ppm), P_2 (−5.8 ppm), P_3 (−24.3 ppm) and P_4 (−20.1 ppm).

In Fig. 5, we show a series of 2D spectra of $AlPO_4$-14 acquired using the general schemes shown in Figs. 1 and 2. Owing to the long T_1 relaxation of ^{31}P nuclei, only the experiments starting from ^{27}Al, i.e., corresponding to $I = {}^{27}Al$ and $S = {}^{31}P$ in R-INEPT, and to $I = {}^{31}P$ and $S = {}^{27}Al$ in HMQC, could be carried out in a reasonable amount of time. The R-INEPT (Fig. 5a) and HMQC (Fig. 5b) experiments were performed at 9.4 T under identical experimental conditions. Site Al_1 is very broad under MAS, and thus hardly observable at 9.4 T (Figs. 5a and b). The resolution in ^{27}Al dimension was enhanced by a factor of about four by recording the same spectra at 18.8 T

shown in Figs. 5c and d. The MQ-*J*-HETCOR spectrum of the same sample obtained at 18.8 T is shown in Fig. 5e. Finally, the MQ-*D*-HETCOR experiment, based on dipolar cross polarization, is shown in Fig. 5f for comparison. The sensitivity of MQMAS-based spectra was enhanced by using soft-pulse added mixing (SPAM) [70], which can be implemented in the MQ-HETCOR methods in a straightforward manner [71]. Also, simultaneous ^{27}Al and ^{1}H CW decoupling was used in these experiments [69] to maximize the resolution in ^{31}P dimension.

The experimental procedures and interpretation of these spectra were detailed in our earlier reports [40,71]. Herein, we call attention to some of the features associated with the presented theory. We first note that ^{31}P resolution observed in the spectra involving R-INEPT (Figs. 5a, c, and e) and CP (Fig. 5f) is much better than for HMQC (Figs. 5b and d). This is because in the latter case only the CT transitions are manipulated by the selective π pulse, whereas the dephasing due to $J_{Al\text{-}P}$ scalar interactions associated with ST's affects the resolution along the F_1 (^{31}P) dimension. This broadening may further increase for nuclei with a higher spin value, such as ^{93}Nb [72]. It can be avoided by starting the HMQC scheme with spin-1/2 nuclei, if their T_1 relaxation permits.

The through bond Al-P connectivities established previously for $AlPO_4$-14 [34,40,67–69] (Al_1 {$1P_1$, $1P_2$, $1P_3$, $1P_4$}, Al_2 {$2P_1$, $1P_2$, $1P_4$}, Al_3 {$1P_1$, $2P_3$, $1P_4$} and Al_4 {$2P_2$, $1P_3$, $1P_4$}) are evident in the MQ-*J*-HETCOR spectrum (Fig. 5e). Only one expected resonance (Al_1–P_2) is not visible due to low intensity, however we have detected it earlier using the same method at 14.1 T [40,71]. More generally, the cross-peaks associated with five- (Al_1) and six- (Al_4) coordinated aluminum sites are notably less intense than those associated with four-coordinated sites Al_2 and Al_3. Several possible factors may have contributed to this result. First, the MQMAS method in itself is not quantitative. However, this is not the dominant cause here, because all expected intensities are well represented in the MQ-*D*-HETCOR spectrum of Fig. 5f. Since the spectral distortions are also severe in Figs. 5a–d, their origin must be attributed to the polarization transfer. Indeed, the results shown in Section 2.1.1.2 show that the efficiency and optimum delays of R-INEPT transfer depend very strongly on C_Q. Al_1 site is submitted to the strongest quadrupole interaction ($C_Q = 5.6$ MHz) and numerical simulations performed with PULSAR [66] showed that the related second-order interaction (not taken into account in our analytical calculations) is certainly the origin of the very weak Al_1–P_2 cross-peak. Additional intensity drop to Al_1 and Al_4 cross-peaks is caused by transverse relaxation, which is enhanced by the water molecules that are attached to these atoms.

4. Conclusion

We have analyzed and compared the HMQC and R-INEPT hetero-nuclear through bond transfers in multi-spin systems involving quadrupolar nuclei in liquid and solid samples. This analysis has lead to generalization of previous formalisms to multi-spin systems SI_n ($n \leqslant 4$) consisting of spin-1/2 or half-integer quadrupolar nuclei. The theoretical predictions of signal intensities and optimization conditions are given for strong and weak quadrupolar interactions.

Some of the theoretical results were verified experimentally using ^{27}Al–^{31}P spin pairs under MAS and MQMAS. A number of factors determine the overall sensitivity of these techniques. In general, the experiments should be arranged such that the fast relaxing nuclei (in our samples ^{27}Al) control the recycle delay. In such case, the HMQC method has the advantage over R-INEPT in that it uses a smaller number of pulses at the ^{27}Al resonance frequency. On the other hand, the observed resolution was lower in the ^{31}P dimension of HMQC. In the absence of transverse relaxation, the delays involved in magnetization transfer are similar in both methods, although only the *S* spin coherences (again, in this case ^{27}Al) are affected during HMQC transfers. In the end, ^{27}Al–^{31}P HETCOR spectra of $AlPO_4$-14 recorded using these two methods exhibited comparable intensities. However, the outcome may be very different for spin pairs with different magnetogyric ratios, quadrupolar interactions and relaxation properties. A major advantage of R-INEPT is that it can be combined with MQMAS or STMAS into a simple 2D experiment, MQ/ST-*J*-HETCOR. This experiment has a similar intrinsic efficiency than the method based on CP dipolar transfer (MQ/ST-*D*-HETCOR), which in $AlPO_4$-14 appeared to be more quantitative. In general, however, the CP-based experiments with quadrupolar nuclei are prone to their own quantitative inaccuracies associated with spin-locking and polarization transfer [42–44]. Whenever possible, both methods should be used to obtain both through-space and through-bond connectivities.

We expect that the double resonance experiments involving *J* coupling will continue to gain popularity as an interesting alternative to CP-based techniques, especially with the increasing availability of higher magnetic fields. The 2D HETCOR spectra shown in Figs. 5a–d exemplify the improvement in sensitivity and resolution observed in the spectra taken at 18.8 T versus those acquired at 9.4 T. We have observed similar results for several other samples studied in our laboratories at 9.4, 14.1 and 18.8 T. Our experience also shows that the MAS spectra of quadrupolar nuclei acquired at 14.1 or 18.8 T can become as simple as those measured at 9.4 T under MQMAS. In such cases, the high-field HETCOR measurements may eliminate the need for MQMAS and STMAS, which further increases the time-saving factor. For example, typical ^{27}Al–^{31}P R-INEPT-based HETCOR spectra obtained in our laboratories under MAS at 14.1 T in 30 min have better S/N and comparable resolution in both dimensions to the

MQMAS-based spectra obtained at 9.4 T in 48 h. Taking into account a 20% efficiency of MQMAS, which is typical for ^{27}Al nuclei, the Zeeman factor and the narrowing of the central transition, an incredible time-saving factor of more than two orders of magnitude is expected. Indeed, we have recently concluded a *J*-based HETCOR study of P-ZSM-5 industrial catalysts with Si/Al ratio of 50 and widely distributed resonances in ^{31}P and ^{27}Al dimensions [73].

Acknowledgments

J.P.A and J.T. thank Region Nord/Pas de Calais, Europe (FEDER), CNRS, French Minister of Science, USTL, ENSCL and the Bruker company for funding. At the Ames Laboratory, this research was supported by the U.S. DOE, Office of BES, under contract W-7405-Eng-82. The authors also thank Drs B.C. Gerstein, D. Massiot and L. Delevoye for helpful discussions.

Appendix A

The 2D HMQC signals observed for SI_n spin system, where $I = S = 1/2$, are as follows:

$$SI: s(t_1,t_2)\beta^{-1} \approx c_{J1}^2(0Q) - s_{J1}^2\cos(2\pi\nu_{I1}t_1)(\pm 1Q) \tag{A1}$$

$$\begin{aligned} SI_2: \quad & s(t_1,t_2)\beta^{-1} \\ & \approx \{c_{J1}^2c_{J2}^2 + 0.5s_{J1}^2s_{J2}^2\cos[2\pi(\nu_{I1}-\nu_{I2})t_1]\}(0Q) \\ & \quad - \{s_{J1}^2c_{J2}^2\cos(2\pi\nu_{I1}t_1) \\ & \quad + s_{J2}^2c_{J1}^2\cos(2\pi\nu_{I2}t_1)\}(\pm 1Q) \\ & \quad + 0.5s_{J1}^2s_{J2}^2\cos[2\pi(\nu_{1I}+\nu_{I2})t_1](\pm 2Q) \end{aligned} \tag{A2}$$

$$\begin{aligned} SI_3: \quad & s(t_1,t_2)\beta^{-1} \\ & \approx \{c_{J1}^2c_{J2}^2c_{J3}^2 + 0.5s_{J1}^2s_{J2}^2c_{J3}^2\cos[2\pi(\nu_{I1}-\nu_{I2})t_1] \\ & \quad + 0.5s_{J1}^2s_{J3}^2c_{J2}^2\cos[2\pi(\nu_{I1}-\nu_{I3})t_1] \\ & \quad + 0.5s_{J2}^2s_{J3}^2c_{J1}^2\cos[2\pi(\nu_{I2}-\nu_{I3})t_1]\}(0Q) \\ & \quad - \{s_{J1}^2c_{J2}^2c_{J3}^2\cos(2\pi\nu_{I1}t_1) \\ & \quad + s_{J2}^2c_{J1}^2c_{J3}^2\cos(2\pi\nu_{I2}t_1) \\ & \quad + s_{J3}^2c_{J1}^2c_{J2}^2\cos(2\pi\nu_{I3}t_1) \\ & \quad + 0.25s_{J1}^2s_{J2}^2s_{J3}^2[\cos(2\pi(\nu_{I1}+\nu_{I2}-\nu_{I3})t_1) \\ & \quad + \cos(2\pi(\nu_{I1}+\nu_{I3}-\nu_{I2})t_1) \\ & \quad + \cos(2\pi(\nu_{I2}+\nu_{I3}-\nu_{I1})t_1)]\}(\pm 1Q) \\ & \quad + \{0.5s_{J1}^2s_{J2}^2c_{J3}^2\cos[2\pi(\nu_{1I}+\nu_{I2})t_1] \\ & \quad + 0.5s_{J1}^2s_{J3}^2c_{J2}^2\cos[2\pi(\nu_{I1}+\nu_{I3})t_1] \\ & \quad + 0.5s_{J2}^2s_{J3}^2c_{J1}^2\cos[2\pi(\nu_{I2}+\nu_{I3})t_1]\}(\pm 2Q) \\ & \quad - 0.25s_{J1}^2s_{J2}^2s_{J3}^2\cos[2\pi(\nu_{I1}+\nu_{I2}+\nu_{I3})t_1](\pm 3Q) \end{aligned} \tag{A3}$$

$$\begin{aligned} SI_4: \quad & s(t_1,t_2)\beta^{-1} \\ & \approx \{c_{J1}^2c_{J2}^2c_{J3}^2c_{J4}^2 + 0.5s_{J1}^2s_{J2}^2c_{J3}^2c_{J4}^2\cos[2\pi(\nu_{I1}-\nu_{I2})t_1] \\ & \quad + 0.5s_{J1}^2s_{J3}^2c_{J2}^2c_{J4}^2\cos[2\pi(\nu_{I1}-\nu_{I3})t_1] \\ & \quad + 0.5s_{J1}^2s_{J4}^2c_{J2}^2c_{J3}^2\cos[2\pi(\nu_{I1}-\nu_{I4})t_1] \\ & \quad + 0.5s_{J2}^2s_{J3}^2c_{J1}^2c_{J4}^2\cos[2\pi(\nu_{I2}-\nu_{I3})t_1] \\ & \quad + 0.5s_{J2}^2s_{J4}^2c_{J1}^2c_{J3}^2\cos[2\pi(\nu_{I2}-\nu_{I4})t_1] \\ & \quad + 0.5s_{J3}^2s_{J4}^2c_{J1}^2c_{J2}^2\cos[2\pi(\nu_{I3}-\nu_{I4})t_1] \\ & \quad + 0.125s_{J1}^2s_{J2}^2s_{J3}^2s_{J4}^2[\cos(2\pi(\nu_{I1}+\nu_{I2}-\nu_{I3}-\nu_{I4})t_1) \\ & \quad + \cos(2\pi(\nu_{I1}+\nu_{I3}-\nu_{I2}-\nu_{I4})t_1) \\ & \quad + \cos(2\pi(\nu_{I1}+\nu_{I4}-\nu_{I2}-\nu_{I3})t_1)]\}(0Q) \\ & \quad - \{s_{J1}^2c_{J2}^2c_{J3}^2c_{J4}^2\cos(2\pi\nu_{1I}t_1) \\ & \quad + s_{J2}^2c_{J1}^2c_{J3}^2c_{J4}^2\cos(2\pi\nu_{I2}t_1) \\ & \quad + s_{J3}^2c_{J1}^2c_{J2}^2c_{J4}^2\cos(2\pi\nu_{I3}t_1) \\ & \quad + s_{J4}^2c_{J1}^2c_{J2}^2c_{J3}^2\cos(2\pi\nu_{I4}t_1) \\ & \quad + 0.25s_{J1}^2s_{J2}^2s_{J3}^2c_{J4}^2[\cos(2\pi(\nu_{I1}+\nu_{I2}-\nu_{I3})t_1) \\ & \quad + \cos(2\pi(\nu_{I1}+\nu_{I3}-\nu_{I2})t_1) \\ & \quad + \cos(2\pi(\nu_{I2}+\nu_{I3}-\nu_{I1})t_1)] \\ & \quad + 0.25s_{J1}^2s_{J2}^2s_{J4}^2c_{J3}^2[\cos(2\pi(\nu_{I1}+\nu_{I2}-\nu_{I4})t_1) \\ & \quad + \cos(2\pi(\nu_{I1}+\nu_{I4}-\nu_{I2})t_1) \\ & \quad + \cos(2\pi(\nu_{I2}+\nu_{I4}-\nu_{I1})t_1)] \\ & \quad + 0.25s_{J1}^2s_{J3}^2s_{J4}^2c_{J2}^2[\cos(2\pi(\nu_{I1}+\nu_{I3}-\nu_{I4})t_1) \\ & \quad + \cos(2\pi(\nu_{I1}+\nu_{I4}-\nu_{I3})t_1) \\ & \quad + \cos(2\pi(\nu_{I3}+\nu_{I4}-\nu_{I1})t_1)] \\ & \quad + 0.25s_{J2}^2s_{J3}^2s_{J4}^2c_{J1}^2[\cos(2\pi(\nu_{I2}+\nu_{I3}-\nu_{I4})t_1) \\ & \quad + \cos(2\pi(\nu_{I2}+\nu_{I4}-\nu_{I3})t_1) \\ & \quad + \cos(2\pi(\nu_{I3}+\nu_{I4}-\nu_{I2})t_1)]\}(\pm 1Q) \\ & \quad + \{0.5[s_{J1}^2s_{J2}^2c_{J3}^2c_{J4}^2\cos(2\pi(\nu_{I1}+\nu_{I2})t_1) \\ & \quad + s_{J1}^2s_{J3}^2c_{J2}^2c_{J4}^2\cos(2\pi(\nu_{I1}+\nu_{I3})t_1) \\ & \quad + s_{J1}^2s_{J4}^2c_{J2}^2c_{J3}^2\cos(2\pi(\nu_{I1}+\nu_{I4})t_1) \\ & \quad + s_{J2}^2s_{J3}^2c_{J1}^2c_{J4}^2\cos(2\pi(\nu_{I2}+\nu_{I3})t_1) \\ & \quad + s_{J2}^2s_{J4}^2c_{J1}^2c_{J3}^2\cos(2\pi(\nu_{I2}+\nu_{I4})t_1) \\ & \quad + s_{J3}^2s_{J4}^2c_{J1}^2c_{J2}^2\cos(2\pi(\nu_{I3}+\nu_{I4})t_1)] \\ & \quad + 0.125s_{J1}^2s_{J2}^2s_{J3}^2s_{J4}^2[\cos(2\pi(\nu_{I1}+\nu_{I2}+\nu_{I3}-\nu_{I4})t_1) \\ & \quad + \cos(2\pi(\nu_{I1}+\nu_{I2}-\nu_{I3}+\nu_{I4})t_1) \\ & \quad + \cos(2\pi(\nu_{I1}-\nu_{I2}+\nu_{I3}+\nu_{I4})t_1) \\ & \quad + \cos(2\pi(-\nu_{I1}+\nu_{I2}+\nu_{I3}+\nu_{I4})t_1)]\}(\pm 2Q) \\ & \quad - 0.25\{s_{J1}^2s_{J2}^2s_{J3}^2c_{J4}^2\cos[2\pi(\nu_{1I}+\nu_{I2}+\nu_{I3})t_1] \\ & \quad + s_{J1}^2s_{J2}^2s_{J4}^2c_{J3}^2\cos[2\pi(\nu_{I1}+\nu_{I2}+\nu_{I4})t_1] \\ & \quad + s_{J1}^2s_{J3}^2s_{J4}^2c_{J2}^2\cos[2\pi(\nu_{I1}+\nu_{I3}+\nu_{I4})t_1] \\ & \quad + s_{J2}^2s_{J3}^2s_{J4}^2c_{J1}^2\cos[2\pi(\nu_{I2}+\nu_{I3}+\nu_{I4})t_1]\}(\pm 3Q) \\ & \quad + 0.125s_{J1}^2s_{J2}^2s_{J3}^2s_{J4}^2\cos[2\pi(\nu_{I1}+\nu_{I2}+\nu_{I3}+\nu_{I4})t_1](\pm 4Q) \end{aligned} \tag{A4}$$

References

[1] R.R. Ernst, G. Bodenhausen, A. Wokaun, Principles of Nuclear Magnetic Resonance in One and Two Dimensions, Clarendon Press, Oxford, 1991.

[2] T. Terao, H. Miura, A. Saika, High-resolution *J*-resolved NMR spectra of dilute spins in solids, J. Chem. Phys. 75 (1981) 1573–1574.

[3] K.W. Zilm, D.M. Grant, High-resolution NMR spectra with *J* couplings in solids, J. Magn. Reson. 48 (1982) 524–526.

[4] R.K. Harris, A. Sebald, High-resolution solid-state ^{119}Sn and ^{207}Pb NMR study of organotin and organolead chalcogenides: observation of *J*-coupling in solids, Magn. Reson. Chem. 27 (1989) 81–87.

[5] P.J. Chu, J.H. Lunsford, D.J. Zalewski, Structural information from the *J*-coupled multiplet of a (trimethylphosphine)trichloroaluminum coordination complex on zeolite Y, J. Magn. Reson. 87 (1990) 68–79.

[6] C.A. Fyfe, K.C. Wong-Moon, Y. Huang, H. Grondey, INEPT experiments in solid-state NMR, J. Am. Chem. Soc. 117 (1995) 10397–10398.

[7] H.-M. Kao, C.P. Grey, INEPT experiments involving quadrupolar nuclei in solids, J. Magn. Reson. 133 (1998) 313–323.

[8] H.-M. Kao, C.P. Grey, Determination of the ^{31}P–^{27}Al *J*-coupling constant for trimethylphosphine bound to the lewis acid site of zeolite HY, J. Am. Chem. Soc. 119 (1997) 627–628.

[9] S.P. Brown, M. Perez-Torralba, D. Sanz, R.M. Claramunt, L. Emsley, Determining hydrogen-bond strengths in the solid state by NMR. The quantitative measurement of homonuclear *J* couplings, Chem. Commun. (2002) 1852–1853.

[10] J. Trebosc, J.P. Amoureux, J.W. Wiench, M. Pruski, Simultaneous frequency-selective solid-state NMR analysis of internuclear distances and through-bond connectivities in the presence of quadrupolar nuclei, Chem. Phys. Lett. 374 (2003) 432–438.

[11] J. Trebosc, J.P. Amoureux, L. Delevoye, J.W. Wiench, M. Pruski, Frequency-selective measurement of heteronuclear scalar couplings in solid-state NMR, Solid State Sci. 6 (2004) 1089–1095.

[12] T. Terao, H. Miura, A. Saika, Simplification and assignment of ^{13}C spectra by using *J*-resolved NMR spectroscopy in solids, J. Am. Chem. Soc. 104 (1982) 5228–5229.

[13] N.C. Nielsen, H. Bildsoee, H.J. Jakobsen, O.W. Soerensen, SEMUT spectral editing and determination of radio-frequency field strengths for ^{13}C cross polarization/magic angle spinning NMR of solids, J. Magn. Reson. 79 (1988) 554–560.

[14] P. Tekely, J. Brondeau, A. Retournard, D. Canet, Partial editing in heteronuclear *J*-resolved solid-state NMR spectroscopy, Magn. Reson. Chem. 27 (1989) 696–698.

[15] D. Sakellariou, A. Lesage, L. Emsley, Spectral editing in solid-state NMR using scalar multiple quantum filters, J. Magn. Reson. 151 (2001) 40–47.

[16] T.A. Early, B.K. John, L.F. Johnson, Observation of homonuclear double-quantum correlations in plastic crystals using cross polarization and magic angle spinning, J. Magn. Reson. 75 (1987) 134–138.

[17] R. Benn, H. Grondey, C. Brevard, A. Pagelot, The detection of connectivities of rare spin-1/2 nuclei in the sold state using natural abundance samples. ^{13}C and ^{29}Si INADEQUATE and COSY type experiments, J. Chem. Soc., Chem. Commun. (1988) 102–103.

[18] C.A. Fyfe, Y. Feng, H. Gies, H. Grondey, G.T. Kokotailo, Natural-abundance two-dimensional solid-state ^{29}Si NMR investigations of three-dimensional lattice connectivities in zeolite structures, J. Am. Chem. Soc. 112 (1990) 3264–3270.

[19] A. Lesage, C. Auger, S. Caldarelli, L. Emsley, Determination of through-bond carbon–carbon connectivities in solid-state NMR using the INADEQUATE Experiment, J. Am. Chem. Soc. 119 (1997) 7867–7868.

[20] S.P. Brown, M. Perez-Torralba, D. Sanz, R.M. Claramunt, L. Emsley, The direct detection of a hydrogen bond in the solid state by NMR through the observation of a hydrogen-bond mediated ^{15}N–^{15}N *J* coupling, J. Am. Chem. Soc. 124 (2002) 1152–1153.

[21] F. Fayon, C. Roiland, L. Emsley, D. Massiot, Triple-quantum correlation NMR experiments in solids using *J*-couplings, J. Magn. Reson. 179 (2006) 49–57.

[22] C.A. Fyfe, H. Gies, Y. Feng, Three-dimensional lattice connectivities from twodimensional high-resolution solid-state NMR. ^{29}Si magic angle spinning NMR investigation of the silicate lattice of zeolite ZSM-39 (Dodecasil 3C), J. Am. Chem. Soc. 111 (1989) 7702–7707.

[23] M. Baldus, B.H. Meier, Total correlation spectroscopy in the solid state. The use of scalar couplings to determine the through-bond connectivity, J. Magn. Reson. A 121 (1996) 65–69.

[24] P. Caravatti, G. Bodenhausen, R.R. Ernst, Heteronuclear solid-state correlation spectroscopy, Chem. Phys. Lett. 89 (1982) 363–367.

[25] D.P. Burum, A. Bielecki, An improved experiment for heteronuclear-correlation 2D NMR in solids, J. Magn. Reson. 94 (1991) 645–652.

[26] B.J. van Rossum, H. Foerster, H.J.M. de Groot, High-field and high-speed CPMAS ^{13}C NMR heteronuclear dipolar-correlation spectroscopy of solids with frequency-switched Lee-Goldburg homonuclear decoupling, J. Magn. Reson. 124 (1997) 516–519.

[27] A.W. Hing, S. Vega, J. Schaefer, J. Magn. Reson. 96 (1992) 205–209.

[28] J.P. Amoureux, M. Pruski, in: D.M. Grant, R.K. Harris (Eds.), Advances in MQMAS NMR, 9, Wiley, London, 2002, pp. 226–251.

[29] S.P. Brown, H.W. Spiess, Advanced solid-state NMR methods for the elucidation of structure and dynamics of molecular, macromolecular, and supramolecular systems, Chem. Rev. 101 (2001) 4125–4155.

[30] J. Trebosc, J.W. Wiench, S. Huh, V.S.Y. Lin, M. Pruski, Studies of organically functionalized mesoporous silicas using heteronuclear solid-state correlation NMR spectroscopy under fast magic angle spinning, J. Am. Chem. Soc. 127 (2005) 7587–7593.

[31] S.J. Opella, Multiple-resonance multi-dimensional solid-state NMR of proteins, Encyclopedia NMR 9 (2002) 427–436.

[32] H. Miura, T. Terao, A. Saika, Heteronuclear two-dimensional *J* spectroscopy in rigid solids, J. Magn. Reson. 68 (1986) 593–596.

[33] M.W. Anderson, J. Klinowski, Monitoring organic products of catalytic reactions on zeolites by two-dimensional *J*-resolved solid-state NMR, Chem. Phys. Lett. 172 (1990) 275–278.

[34] C.A. Fyfe, H. Meyer zu Altenschildesche, K.C. Wong-Moon, H. Grondey, J.M. Chezeau, 1D and 2D solid state NMR investigations of the framework structure of as-synthesized $AlPO_4$-14, Solid State Nucl. Magn. Reson. 9 (1997) 97–106.

[35] A. Lesage, D. Sakellariou, S. Steuernagel, L. Emsley, Carbon-proton chemical shift correlation in solid-state NMR by through-bond multiple-quantum spectroscopy, J. Am. Chem. Soc. 120 (1998) 13194–13201.

[36] D. Massiot, F. Fayon, B. Alonso, J. Trebosc, J.-P. Amoureux, Chemical bonding differences evidenced from *J*-coupling in solid state NMR experiments involving quadrupolar nuclei, J. Magn. Reson. 164 (2003) 160–164.

[37] J.P. Amoureux, J. Trebosc, J.W. Wiench, D. Massiot, M. Pruski, Frequency selective solid state NMR measurement of *J* couplings between spin-1/2 and quadrupolar nuclei, Solid State Nucl. Magn. Reson. 27 (2005) 228–232.

[38] D. Iuga, C. Morais, Z. Gan, D.R. Neuville, L. Cormier, D. Massiot, NMR heteronuclear correlation between quadrupolar nuclei in solids, J. Am. Chem. Soc. 127 (2005) 11540–11541.

[39] M. Deschamps, F. Fayon, V. Montouillout, D. Massiot, Trough-bond homonuclear correlation experiments in solid-state NMR applied to quadrupolar nuclei in Al–O–P–O–Al chains, Chem. Comm (2006) 1924–1925.

[40] J.W. Wiench, M. Pruski, Probing through bond connectivities with MQMAS NMR, Solid State Nucl. Magn. Reson. 26 (2004) 51–55.

[41] L. Frydman, J.S. Harwood, Isotropic spectra of half-integer quadrupolar spins from bidimensional magic-angle spinning NMR, J. Am. Chem. Soc. 117 (1995) 5367–5368.

[42] A.J. Vega, MAS NMR spin locking of half-integer quadrupolar nuclei, J. Magn. Reson. 96 (1992) 50–68.

[43] A.J. Vega, CP/MAS of quadrupolar S = 3/2 nuclei, Solid State Nucl. Magn. Reson. 1 (1992) 17–32.

[44] J.P. Amoureux, M. Pruski, Theoretical and experimental assessment of single and multiple-quantum cross-polarization in solid-state NMR, Mol. Phys. 100 (2002) 1595–1613.
[45] G.A. Morris, R. Freeman, Enhancement of nuclear magnetic resonance signals by polarization transfer, J. Am. Chem. Soc. 101 (1979) 760–762.
[46] Z. Gan, Isotropic NMR spectra of half-integer quadrupolar nuclei using satellite transitions and magic-angle spinning, J. Am. Chem. Soc. 122 (2000) 3242–3243.
[47] G.A. Morris, Sensitivity enhancement in ^{15}N NMR: polarization transfer using the INEPT pulse sequence, J. Am. Chem. Soc. 102 (1980) 428–429.
[48] D.P. Burum, R.R. Ernst, Net polarization transfer via a *J*-ordered state for signal enhancement of low-sensitivity nuclei, J. Magn. Reson. 39 (1980) 163–168.
[49] D.T. Pegg, D.M. Doddrell, W.M. Brooks, M.R. Bendall, Proton polarization transfer enhancement for a nucleus with arbitrary spin quantum number from n scalar coupled protons for arbitrary preparation times, J. Magn. Reson. 44 (1981) 32–40.
[50] O.W. Sørensen, R.R. Ernst, Elimination of spectral distortion in polarization transfer experiments. Improvements and comparison of techniques, J. Magn. Reson. 51 (1983) 477–489.
[51] D.M. Doddrell, D.T. Pegg, M.R. Bendall, Distortionless enhancement of NMR signals by polarization transfer, J. Magn. Reson. 48 (1982) 323–327.
[52] G. Bodenhausen, D.J. Ruben, Natural abundance ^{15}N NMR by enhanced heteronuclear spectroscopy, Chem. Phys. Lett. 69 (1980) 185–189.
[53] A. Bax, R.H. Griffey, B.L. Hawkins, Sensitivity-enhanced correlation of ^{15}N and proton chemical shifts in natural-abundance samples via multiple quantum coherence, J. Am. Chem. Soc. 105 (1983) 7188–7190.
[54] D.T. Pegg, M.R. Bendall, Coupled polarization transfer spectra for higher-spin nuclei, J. Magn. Reson. 58 (1984) 14–26.
[55] D.P. Burum, Heteronuclear correlated 2D NMR spectroscopy of spins greater than 1/2. Application to decaborane, J. Magn. Reson. 59 (1984) 430–436.
[56] C. Zwahlen, P. Legault, S.J.F. Vincent, J. Greenblatt, R. Konrat, L.E. Kay, Methods for measurement of intermolecular NOEs by multinuclear NMR spectroscopy: application to a bacteriophage lN-peptide/boxB RNA complex, J. Am. Chem. Soc. 119 (1997) 6711–6721.
[57] Z. Yao, H.T. Kwak, D. Sakellariou, L. Emsley, P.J. Grandinetti, Sensitivity enhancement of the central transition NMR signal of quadrupolar nuclei under magic-angle spinning, Chem. Phys. Lett. 327 (2000) 85–90.
[58] H.T. Kwak, S. Prasad, Z. Yao, P.J. Grandinetti, J.R. Sachleben, L. Emsley, Enhanced sensitivity in RIACT/MQ-MAS NMR experiments using rotor assisted population transfer, J. Magn. Reson. 150 (2001) 71–80.
[59] P.K. Madhu, A. Goldbourt, L. Frydman, S. Vega, Sensitivity enhancement of the MQMAS NMR experiment by fast amplitude modulation of the pulses, Chem. Phys. Lett. 307 (1999) 41–47.
[60] A.P.M. Kentgens, R. Verhagen, Advantages of double frequency sweeps in static, MAS and MQMAS NMR of spin $I = 3/2$ nuclei, Chem. Phys. Lett. 300 (1999) 435–443.
[61] R. Siegel, T.T. Nakashima, R.E. Wasylishen, Signal enhancement of NMR spectra of half-integer quadrupolar nuclei in solids using hyperbolic secant pulses, Chem. Phys. Lett. 388 (2004) 441–445.
[62] T. Vosegaard, F.H. Larsen, H.J. Jakobsen, P.D. Ellis, N.C. Nielsen, Sensitivity-enhanced multiple-quantum MAS NMR of half-integer quadrupolar nuclei, J. Am. Chem. Soc. 119 (1997) 9055–9056.
[63] R. Lefort, J.W. Wiench, M. Pruski, J.P. Amoureux, Optimization of data acquisition and processing in Carr–Purcell–Meiboom–Gill multiple quantum magic angle spinning nuclear magnetic resonance, J. Chem. Phys. 116 (2002) 2493–2501.
[64] A. Goiffon, J.C. Jumas, M.M. Aurin, E. Philippot, Structure studies of α-quartz type phases of MIIIXVO4 (MIII = Al, Ga and XV = P, As) at temperatures of 172, 293 and 373 K, J. Solid State Chem. 61 (1986) 384–396.
[65] C. Huguenard, F. Taulelle, Z. Gan, Optimizing STMAS, J. Magn. Reson. 156 (2002) 131–137.
[66] J.P. Amoureux, C. Fernandez, Y. Dumazy, A useful tool for the elaboration of new solid-state NMR experiments: PULSAR, J. Chim. Phys. 92 (1995) 1939–1942.
[67] M. Helliwell, V. Kaucic, G.M.T. Cheetham, M.M. Harding, B.M. Kariuki, P.J. Rizkallah, Structure determination from small crystals of two aluminophosphates CrAPO-14 and SAPO-43, Acta Crystallogr. B49 (1993) 413–420.
[68] C. Fernandez, J.P. Amoureux, J.M. Chezeau, L. Delmotte, H. Kessler, ^{27}Al MAS NMR characterization of $AlPO_4$-14. Enhanced resolution and information by MQMAS, Micropor. Mat. 6 (1996) 331–340.
[69] L. Delevoye, C. Fernandez, C.M. Morais, J.-P. Amoureux, V. Montouillout, J. Rocha, Double-resonance decoupling for resolution enhancement of ^{31}P solid-state MAS and ^{27}Al–^{31}P MQHETCOR NMR, Solid State Nucl. Magn. Reson. 22 (2002) 501–512.
[70] Z. Gan, H.-T. Kwak, Enhancing MQMAS sensitivity using signals from multiple coherence transfer pathways, J. Magn. Reson. 168 (2004) 346–351.
[71] J.W. Wiench, G. Tricot, L. Delevoye, J. Trebosc, J. Frye, L. Montagne, J.-P. Amoureux, M. Pruski, SPAM-MQMAS-HETCOR: an improved method for heteronuclear spectroscopy between quadrupolar and spin-1/2 nuclei in solid-state NMR, Phys. Chem. Chem. Phys. 8 (2000) 144–150.
[72] L.S. Du, R.W. Schurko, K.H. Lim, C.P. Grey, A solid-state ^{93}Nb and ^{19}F NMR spectroscopy and XR diffraction study of potassium heptafluoro-niobate (V): characterization of ^{93}Nb, ^{19}F coupling, and fluorine motion, J. Phys. Chem. A105 (2001) 760–768.
[73] K. Damodaran, J.W. Wiench, S.M. Cabral de Menezes, Y.L. Lam, J. Trebosc, J.-P. Amoureux, M. Pruski, Modification of H-ZSM-5 zeolites with phosphorus. 2. Interaction between phosphorus and aluminum studied by solid-state NMR spectroscopy, Micropor. Mesopor. Mater. xxx (2006) 297–306.